








RESEARCH ARTICLE

10.1029/2023SW003780

A Substorm-Dependent Negative Limit of Non-Eclipse Surface Charging of a Chinese Geosynchronous Satellite

Zhiyi Fu^{1,2,3} , Zhenpeng Su^{1,2,3} , Bin Miao^{1,2,3}, Zhiyong Wu^{1,2,3} , Yiren Li^{1,2,3} , Kai Liu^{1,2,3}, Xu Shan⁴, and Yuming Wang^{1,2,5} 

Key Points:

- Negative surface charging potentials are inferred from ion energy spectrograms for a Chinese geosynchronous navigation satellite
- Non-eclipse extreme negative surface charging occurs primarily from pre-midnight through dawn to pre-noon magnetic local times
- Non-eclipse surface charging potentials have a negative limit determined by substorm strength

¹Deep Space Exploration Laboratory, School of Earth and Space Sciences, University of Science and Technology of China, Hefei, China, ²CAS Center for Excellence in Comparative Planetology, CAS Key Laboratory of Geospace Environment, Mengcheng National Geophysical Observatory, University of Science and Technology of China, Hefei, China, ³Collaborative Innovation Center of Astronautical Science and Technology, Harbin, China, ⁴Hefei National Research Center for Physical Sciences at the Microscale, Department of Modern Physics, University of Science and Technology of China, Hefei, China, ⁵Hefei National Laboratory, University of Science and Technology of China, Hefei, China

Correspondence to:

Z. Su and X. Shan,
szpe@mail.ustc.edu.cn;
xshan@ustc.edu.cn

Citation:

Fu, Z., Su, Z., Miao, B., Wu, Z., Li, Y., Liu, K., et al. (2024). A substorm-dependent negative limit of non-eclipse surface charging of a Chinese geosynchronous satellite. *Space Weather*, 22, e2023SW003780. <https://doi.org/10.1029/2023SW003780>

Received 2 NOV 2023
Accepted 16 JAN 2024

Abstract Surface charging is one of the most common causes of spacecraft anomalies. When and to what potential the spacecraft is charged are two important questions in space weather. Here, for a Chinese geosynchronous navigation satellite, we infer the extreme negative surface charging potentials from the ion differential fluxes measured by a low-energy ion spectrometer. Without the solar eclipse effect away from the midnight, the charging potentials are found to have a negative limit which is determined by the maximum SuperMAG electrojet index in the preceding 2 hr. Such an empirical relation can be reasonably explained by the dependence of 1–50 keV electron fluxes on substorm strength. Similar relations may also exist for other inner magnetospheric spacecraft in the non-eclipse region, which would be useful for spacecraft engineering and space weather alerts.

Plain Language Summary Spacecraft charging is the charging of spacecraft surfaces or components relative to the surrounding space plasma. There have been numerous reports of serious spacecraft anomalies related to the surface charging. When and to what potential the spacecraft is charged are two important questions in space weather. For a Chinese navigation satellite in the geosynchronous orbit, we show that the non-eclipse charging potentials have a negative limit determined by the maximum SuperMAG electrojet index in the preceding 2 hr. Such an empirical relation can be reasonably explained by the dependence of 1–50 keV electron fluxes on substorm strength. For other magnetospheric spacecraft, similar relations may also exist and would be useful for spacecraft engineering and space weather alerts.

1. Introduction

Spacecraft charging is the charging of spacecraft surfaces or components relative to the surrounding space plasma. This can lead to discharges and even catastrophic anomalies (Choi et al., 2011; Ganushkina et al., 2021; Lanzerotti et al., 1998; Loto'aniu et al., 2015; Reagan et al., 1983; Rosen, 1976). When and to what potential the spacecraft is charged are two important questions in space weather.

In general, spacecraft charging can be classified into surface and internal charging (Czepiela et al., 2000; Reagan et al., 1983). There have been numerous reports of serious spacecraft anomalies related to the surface charging (Choi et al., 2011; Ganushkina et al., 2021; Koons et al., 1999; Matéo-Vélez et al., 2018). The surface charging is a result of the imbalance between currents exiting and entering the surface (Berry Garrett, 1981; Lai & Tautz, 2006b). In the environmental plasma of thermal equilibrium, compared to ions, electrons have much larger velocities and are easier to attach to the surface (Lai, 2003; Lai & Della-Rose, 2001; Reagan et al., 1983). In the inner magnetosphere, the enhancements of electrons with energies above keV have been found to cause the high negative surface charging (Lai & Tautz, 2006a; Mullen et al., 1986; Olsen, 1983; Sarno-Smith et al., 2016; Thomsen et al., 2013). These electrons are primarily injected by substorms into the region from midnight to dawn-side (DeForest & McIlwain, 1971; Forsyth et al., 2016; Ganushkina et al., 2021; Meredith et al., 2004; Moore et al., 1981; Thomsen et al., 2007). When solar photons with sufficiently high energies strike the surface materials, photoelectrons are emitted from the surface (Grard et al., 1983). In the eclipse region where the sunlight has been blocked by the Earth, spacecraft are more likely to be charged to extremely high negative potentials (Berry Garrett, 1981; Matéo-Vélez et al., 2018; Mullen et al., 1981; Sarno-Smith et al., 2016). Given the cascading

© 2024. The Authors.

This is an open access article under the terms of the [Creative Commons Attribution-NonCommercial-NoDerivs License](https://creativecommons.org/licenses/by/4.0/), which permits use and distribution in any medium, provided the original work is properly cited, the use is non-commercial and no modifications or adaptations are made.

causal relationships of substorms, energetic electrons, and negative surface charging described above, a natural question arises as to whether it is possible to develop an empirical relation between the non-eclipse surface charging potential and the substorm activity strength.

In this study, we concentrate on the surface charging of a Chinese navigation satellite in the geosynchronous orbit. We show that the surface charging potentials inferred from the measurements of ion differential fluxes by the Low Energy Ion Spectrometer (LEIS) (Shan et al., 2023a, 2023b) have a substorm-dependent negative limit in the non-eclipse region.

2. Inference of Surface Charging Potentials

Onboard the satellite, the LEIS instrument can measure the ion fluxes in the energy range of 0.05–25 keV/q over a large field of view of 360° azimuthal angles and 90° elevation angles (Shan et al., 2023a, 2023b). The elevation angles of incident ions are determined by the deflector voltages, and the incident ions of different azimuthal angles are counted at 16 channels (numbered from Ch00 to Ch15). These data have a time resolution Δt of 20 s and a relative energy resolution $\frac{\Delta E_k}{E_k}$ of 8.5%.

Figures 1a–1d show examples of ion differential fluxes recorded by Ch05, Ch01, Ch09, and Ch13 of LEIS from 15:00 UT to 21:00 UT on 14 October 2021. Ch01, Ch05, Ch09, and Ch13 are evenly distributed over the azimuthal angle range of 0°–360°. Because of the obstruction of view by other spacecraft components, these ion spectrograms exhibited periodic gaps (Shan et al., 2023a). Clearly, the obstruction effect was weakest for Ch05. The extreme enhancement of ion fluxes in a narrow range of energy bins appears like a bright yellow line, which is an indicator of negative surface charging (DeForest, 1972; Sarno-Smith et al., 2016; Thomsen et al., 2013). The low-energy ions are accelerated by the negative potentials when crossing the spacecraft sheath and then the recorded high-energy ion fluxes exhibit an enhancement (Thomsen et al., 2007, 2013). Near the detector, the spacecraft surface may be charged differentially relative to the detector. The differential charging could cause the focusing of ion fluxes and the formation of feathered structures above the ion charging lines, particularly for Ch13 (Berry Garrett, 1981; DeForest, 1972). Given that the background ions are mainly protons, the charging potential absolute $|U_s|$ approximately equals the energy E_k of the bright line divided by the unit charge e . $|U_s|$ reached ~3,900 V near the midnight around 16:19 UT and fell to ~400 V in the post-midnight region after 17:00 UT. As illustrated in the previous studies (Ferguson et al., 2015; Grard et al., 1983; Matéo-Vélez et al., 2018), the geosynchronous spacecraft experiences the solar eclipses around the midnight near the equinoxes. In this event, the solar eclipse may be the primary cause of extreme negative surface charging around 16:19 UT, and the substorm injection may be responsible for the rest charging.

We have developed an algorithm to automatically recognize the extreme charging events ($|U_s| > 100$ V). This algorithm involves the ion count rate n_i , the normalized energy gradient \bar{C}_i of n_i

$$\bar{C}_i = \frac{C_i}{\max(C_j, j = 1, 2, 3, \dots)}, \quad (1)$$

$$C_i = \left| \frac{n_i - n_{i-1}}{\log E_{k,i} - \log E_{k,i-1}} \right|, \quad (2)$$

and the ion flux j_i , where the suffix i denotes the i th energy bin $E_{k,i}$. At a specific time moment, we identify the energy bin forming the charging line with two procedures. First, we identify the minimum energy bin $E_{k,i}$ with $\bar{C}_i > 0.7$ and $n_i > 20$, below which the maximum value of \bar{C}_i is less than 0.2 and the average value of \bar{C}_i is less than 0.1. If no energy bins are identified from the first procedure, we perform the second procedure to identify the minimum energy bin $E_{k,i}$ with $j_i > 10^8 \text{ cm}^{-2} \text{ s}^{-1} \text{ sr}^{-1} \text{ keV}^{-1}$. These procedures generally help recognize the lower energy edge of the charging line, which the cold ions are most likely accelerated to. Figure 1e shows the derived $|U_s|$ values from all the channels in this event. Most of the time, these channels gave roughly consistent evaluation on the spacecraft potential. At certain time moments, because of the existence of feathered structures related to the sheath focusing effect, the relative difference of these identified charging potentials with respect to the Ch05 values can reach 13% when $|U_s| > 1,000$ V and 30% when $|U_s| < 500$ V.

Considering that Ch05's field of view was less obstructed and its sheath focusing effect was relatively weak, we statistically analyze the data of Ch05. Using the algorithm described above, we have found 4068 extreme

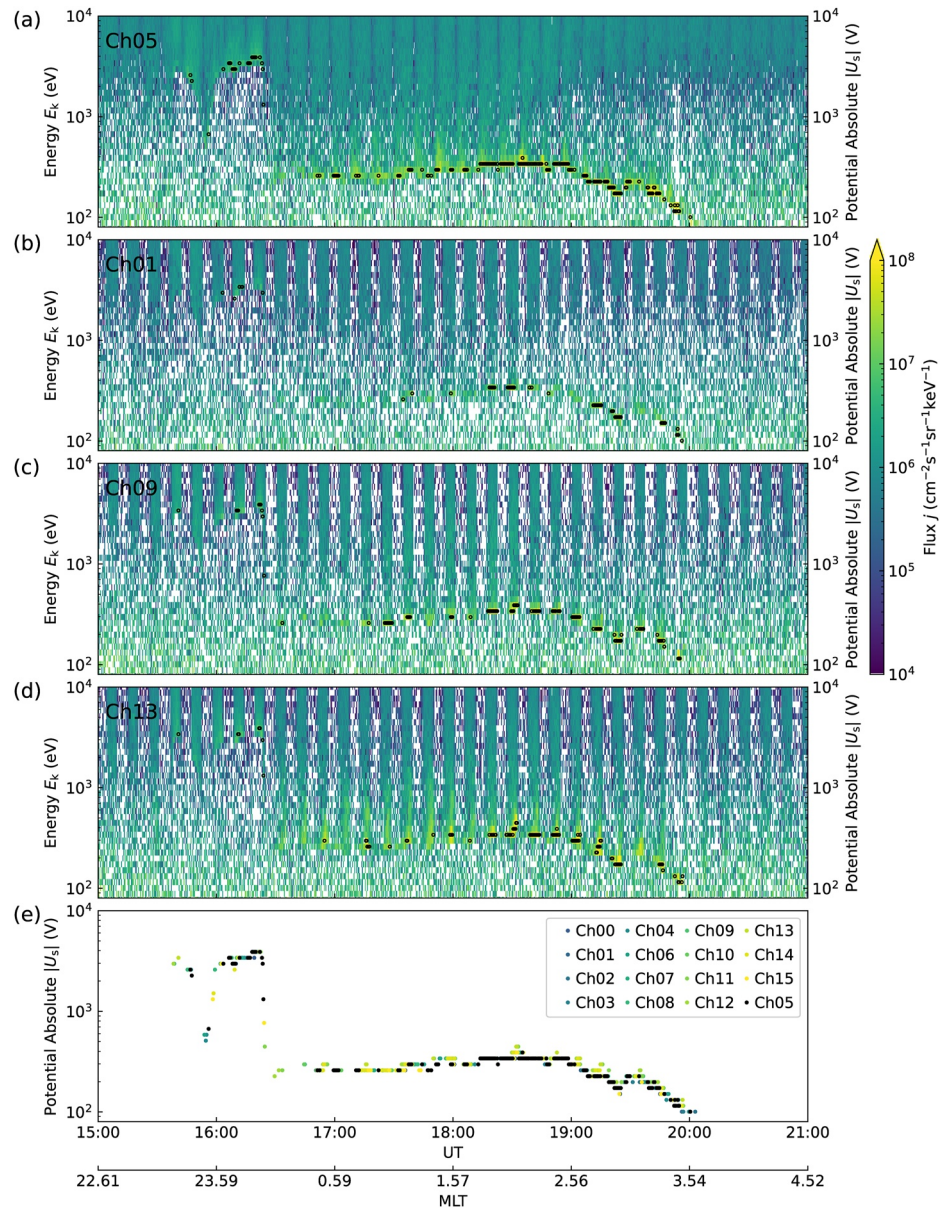


Figure 1. Ion differential fluxes and charging potentials from 15:00 UT to 21:00 UT on 14 October 2021. (a–d) Ion differential fluxes j (color-coded) recorded by the Ch05, Ch01, Ch09, and Ch13 channels. The black circles mark the negative surface charging events identified automatically. (e) Charging potential absolutes $|U_s|$ from all the 16 channels. Colors help differentiate among these channels.

charging events from 24 September 2021 to 25 May 2023 (with a data gap related to the latch-up in the LEIS electronics from 09 May 2022 to 28 December 2022). These extreme charging events ($|U_s| > 100$ V) are scattered over 133 days.

3. Surface Charging Magnitudes, Locations, and Timings

Figure 2 shows the distribution of charging events in terms of magnitude, location, and time. As shown in Figure 2a, the surface charging of this navigation satellite occurs mainly over the magnetic local time (MLT) from 20:00 through 00:00 to 09:00, consistent with previous results for the Los Alamos National Laboratory (LANL) geosynchronous satellites (Thomsen et al., 2013). We further classify these events into two groups according to their occurring MLTs. One group is located at $MLT = 22.5\text{--}0.5$, whose potentials $|U_s|$ extend to 10^4 V. Charging

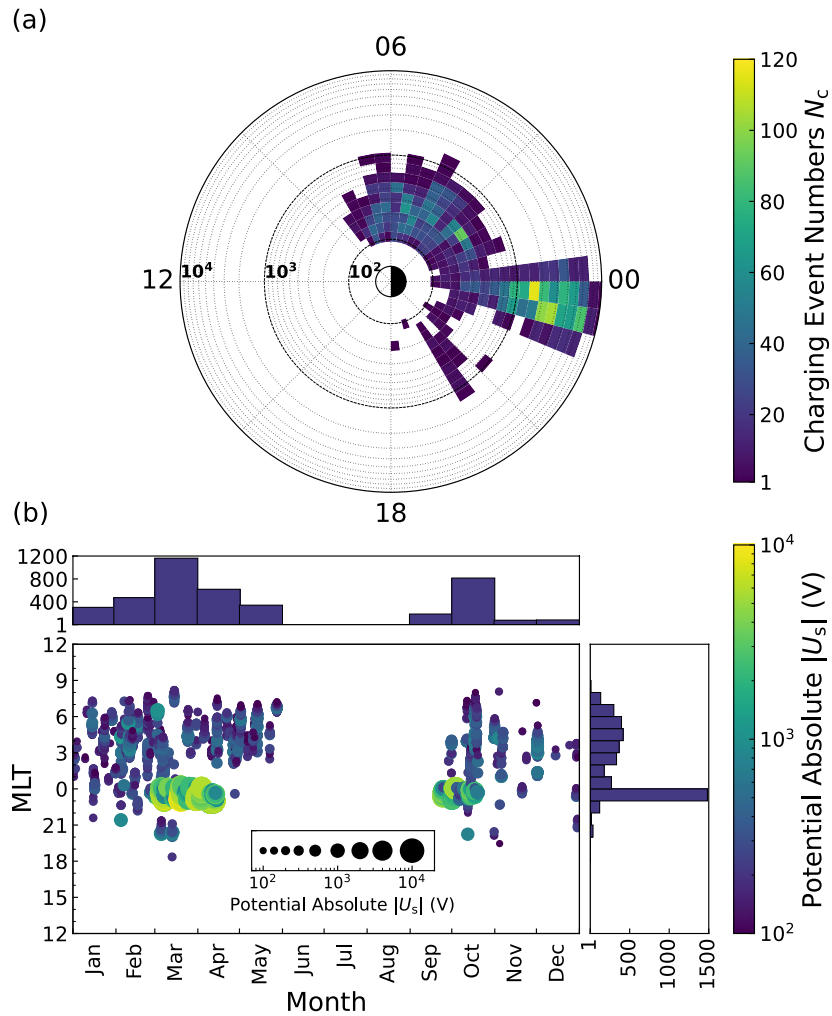


Figure 2. Magnitudes, locations, and timings of surface charging. (a) Extreme negative charging event number N_c (color-coded) as a function of potential absolute $|U_s|$ and magnetic local time (MLT). The radial direction represents $|U_s|$ and the azimuthal direction represents MLT. (b) Scatter plot of extreme negative charging events in the MLT-month plane, with the side panels representing the number of events contained within each interval. The color and size of each point are coded according to $|U_s|$. Note that our data has a gap approximately from June to August.

events with $|U_s| > 2 \times 10^3$ V in this group gather near the equinoxes (Figure 2b) and could be triggered by the solar eclipses (Ferguson et al., 2015; Grard et al., 1983; Matéo-Vélez et al., 2018). In contrast, the other group has a lower charging potential limit and occurs primarily in the region counterclockwise from $MLT = 0.5$ to $MLT = 9$. This group should be free from the solar eclipse effect and be directly related to the substorm injection. These spatial distribution characteristics of the eclipse and non-eclipse events are generally consistent with those for the Van Allen Probes (Mauk et al., 2013; Sarno-Smith et al., 2016). The significant MLT asymmetry of non-eclipse events should be a result of electron drift in the magnetosphere. A statistical study (Li et al., 2010) has shown that the MLT asymmetry of electron fluxes decreases with the increase of energies. These non-eclipse charging could be caused primarily by electrons with energies from keV to tens of keV (Li et al., 2010).

4. Substorm Dependent Negative Limit of Charging Potentials

The substorm activities are characterized by the SuperMAG electrojet (SME) index (Gjerloev, 2012; Newell & Gjerloev, 2011). SME index is the SuperMAG generalization of the traditional auroral electrojet (AE) index. Different from AE based on the measurements of 12 ground-based magnetometer stations, SME is evaluated with more than 100 stations. Considering the drift and accumulation of substorm-injected electrons, we introduce

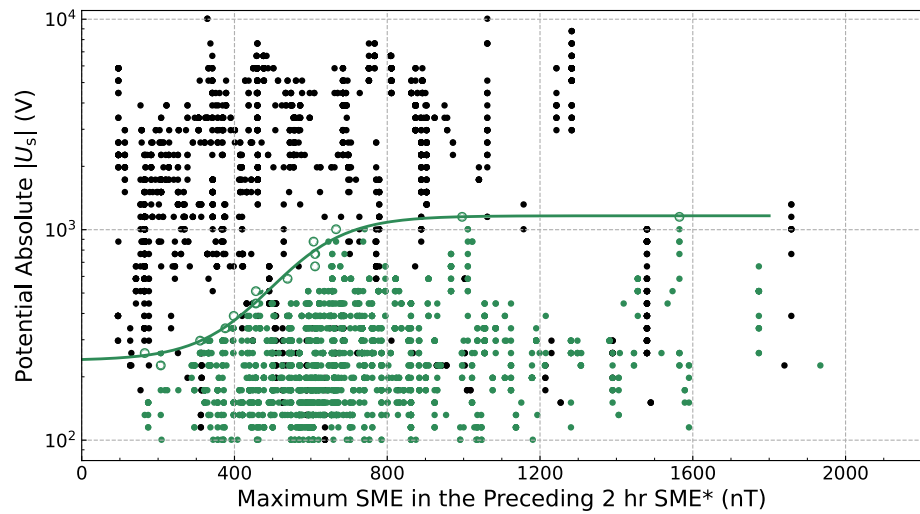


Figure 3. Scatter plot of extreme negative surface charging events in the $|\overline{U}_s|$ -SME* plane, with the black color for the events near the midnight (MLT = 22.5–0.5) and the green color for the events away from the midnight (MLT = 18–22.5 and MLT = 0.5–9). The green line represents a nonlinear fit to the upper potential limit (green circles) of the events away from the midnight.

SME*, the maximum SME in the preceding 2 hr. Figure 3 presents a scatter plot of 4068 charging events in the $|\overline{U}_s|$ - SME* plane. Near the midnight (MLT = 22.5–0.5), the charging potentials $|\overline{U}_s|$ appear to be distributed irregularly. This feature is reasonable because both the solar eclipse effect and substorm activities could contribute to the surface charging. In contrast, away from the midnight, the non-eclipse events are related to the substorm-injected electrons. The corresponding charging potentials $|\overline{U}_s|$ have an upper limit $|\overline{U}_s|$ controlled by SME*. Specifically, when $300 \text{ nT} < \text{SME}^* < 800 \text{ nT}$, the logarithm of potential upper limit $\log |\overline{U}_s|$ increases approximately linearly with SME*; when $\text{SME}^* > 800 \text{ nT}$, $|\overline{U}_s|$ visually reaches a saturation level of $1.3 \times 10^3 \text{ V}$. Overall, we can obtain a simple relation between $|\overline{U}_s|$ and SME*

$$|\overline{U}_s| = 10^{c_1 \tanh \frac{\text{SME}^* - c_2}{c_3} + c_4} \text{ V}, \quad (3)$$

with the fitting parameters c_1 , c_2 , c_3 , and c_4 and the determination coefficient R^2 listed in Table 1. For the events near the midnight, we cannot accurately differentiate between the contributions of solar eclipse and substorm injection. Intuitively, the substorm injection effect may not vary steeply within several hours of MLT around the midnight. Thomsen et al. (2013) had shown that, for the LANL satellites, the months away from equinoxes have approximately the same probability of charging potential $< -100 \text{ V}$. We speculate that the black dots below the green line represent the same charging characteristic as the green dots and both are mainly controlled by the substorm injection. With the addition of solar eclipse effect, the charging potentials would be able to exceed the negative limit related to the substorm injection.

The $|\overline{U}_s|$ -SME* Relation 3 described above can be reasonably explained by the substorm-dependence of energetic electron fluxes. Figure 4 shows the SME*-dependent distribution of 1, 10, and 50 keV electron fluxes j measured by the Van Allen Probes (Blake et al., 2013; Funsten et al., 2013; Spence et al., 2013) from MLT = 0

Table 1 Fitting Parameters and Determination Coefficients of the $ \overline{U}_s $ -SME* and \overline{j} -SME* Relations Defined in Equations 3 and 4						
Name		c_1	c_2 (nT)	c_3 (nT)	c_4	R^2
Charging Potential		0.34380	495.03	198.90	2.7223	0.96941
Electron Flux	1 keV	0.021213	439.27	266.95	0.81318	0.98872
	10 keV	0.75240	-1,258.9	686.99	0.0023428	0.94154
	50 keV	0.046832	196.18	291.53	0.65568	0.98295

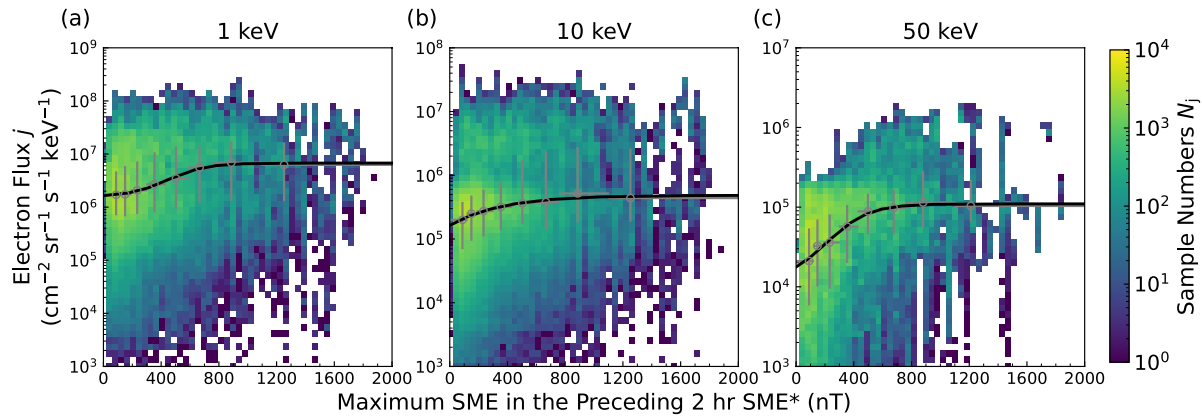


Figure 4. SME*-dependent electron differential fluxes j at (a) 1, (b) 10, and (c) 50 keV measured by the Van Allen Probes from MLT = 0 to MLT = 9 near the geosynchronous orbit during the time range from November 2012 to July 2019. These data have been divided into 8 intervals of SME*: 0–120 nT, 120–190 nT, 190–300 nT, 300–430 nT, 430–590 nT, 590–760 nT, 760–1,100 nT, and 1,100–2,000 nT. In each SME* interval (gray horizontal line), the geometric mean \bar{j} (gray circle) and the corresponding upper and lower quartiles (gray vertical line) have been calculated. The black lines represent a nonlinear fit to the obtained geometric means of electron fluxes.

to MLT = 9 near the geosynchronous orbit during the time range from November 2012 to July 2019. We have divided these data into 8 intervals of SME* and then calculate the geometric mean \bar{j} in each interval. It is obvious that, at every energy bin, \bar{j} exhibits a SME*-dependence analogous to $|\overline{U_s}|$. Specifically, there is a monotonic increase of \bar{j} when SME* < 800 nT and a saturation of \bar{j} when SME* > 800 nT. Similar to $|\overline{U_s}|$, \bar{j} can be fitted to a SME*-dependent function

$$\bar{j} = 10^{c_1 \tanh \frac{\text{SME}^* - c_2}{c_3} + c_4} \text{ cm}^{-2} \text{ s}^{-1} \text{ sr}^{-1} \text{ keV}^{-1}, \quad (4)$$

with the fitting parameters and determination coefficients listed in Table 1.

5. Summary

This study sets out to develop an empirical relation between substorm strength and spacecraft surface charging potential in the non-eclipse region. For the Chinese satellite in the geosynchronous orbit, we infer the extreme negative charging potentials from the charging lines in the ion energy spectrograms measured by the LEIS instrument. The 4068 charging events with the potential absolutes $|U_s| > 100$ V can be classified into two groups: (a) the events close to the midnight, whose charging potentials have been affected by the solar eclipses near the equinoxes, and (b) the other events away from the midnight, whose charging potential absolutes have an upper limit $|\overline{U_s}|$ determined by the maximum SuperMAG electrojet index in the preceding 2 hr SME*. This simple $|\overline{U_s}|$ -SME* relation for the non-eclipse events can be reasonably explained by the dependence of 1–50 keV electron fluxes on SME*. Spacecraft charging depends on the geometry and material properties of the spacecraft, as well as its orbital characteristics. For other inner magnetospheric spacecraft in the non-eclipse region, similar relations between the negative charging limit and the substorm strength may also exist. These empirical relations would be useful for spacecraft engineering and space weather alerts.

Data Availability Statement

LEIS data are available at DREAMS Website (2023). Van Allen Probes data are available at NASA's Space Physics Data Facility (SPDF) Website (2023). We have analyzed the following Van Allen Probes data: HOPE electron flux data (Funsten, 2022) and MagEIS electron flux data (Spence et al., 2022). SME index is available at SuperMAG Website (2023).

Acknowledgments

We acknowledge all the collaborators from the Shandong Institute of Space Electronic Technology and China Academy of Space Technology for their help in the fabrication and environmental tests of LEIS. We acknowledge ECT teams for the use of Van Allen Probes data and acknowledge the SuperMAG collaborators for the use of SME index. This work was supported by the National Natural Science Foundation of China Grants 42188101, 42274198, and 42074222, and the Key Research Program of the Chinese Academy of Sciences Grant ZDRE-KT-2021-3.

References

Berry Garrett, H. (1981). The charging of spacecraft surfaces. *Reviews of Geophysics and Space Physics*, 19(4), 577–616. <https://doi.org/10.1029/RG019i004p00577>

Blake, J. B., Carranza, P. A., Claudepierre, S. G., Clemmons, J. H., Crain, W. R., Dotan, Y., et al. (2013). The magnetic electron ion spectrometer (MagEIS) instruments aboard the radiation belt storm probes (RBSP) spacecraft. *Space Science Reviews*, 179(1–4), 383–421. <https://doi.org/10.1007/s11214-013-9991-8>

Choi, H.-S., Lee, J., Cho, K.-S., Kwak, Y.-S., Cho, I.-H., Park, Y.-D., et al. (2011). Analysis of GEO spacecraft anomalies: Space weather relationships. *Space Weather*, 9(6), 06001. <https://doi.org/10.1029/2010SW000597>

Czepiela, S. A., McManus, H., & Hastings, D. (2000). Charging of composites in the space environment. *Journal of Spacecraft and Rockets*, 37(5), 556–560. <https://doi.org/10.2514/2.3619>

DeForest, S. E. (1972). Spacecraft charging at synchronous orbit. *Journal of Geophysical Research*, 77(4), 651–659. <https://doi.org/10.1029/JA077i004p00651>

DeForest, S. E., & McIlwain, C. E. (1971). Plasma clouds in the magnetosphere. *Journal of Geophysical Research*, 76(16), 3587–3611. <https://doi.org/10.1029/JA076i016p03587>

DREAMS Website. (2023). Low energy ion spectrometer (LEIS) of Chinese navigation satellite at geosynchronous orbit noise reduced science data. Level 1B count and level 2 energy differential flux data [Dataset]. <https://doi.org/10.12411/LEIS>

Ferguson, D. C., Worden, S. P., & Hastings, D. E. (2015). The space weather threat to situational awareness, communications, and positioning systems. *IEEE Transactions on Plasma Science*, 43(9), 3086–3098. <https://doi.org/10.1109/TPS.2015.2412775>

Forsyth, C., Rae, I. J., Murphy, K. R., Freeman, M. P., Huang, C. L., Spence, H. E., et al. (2016). What effect do substorms have on the content of the radiation belts? *Journal of Geophysical Research: Space Physics*, 121(7), 6292–6306. <https://doi.org/10.1002/2016JA022620>

Funsten, H. O. (2022). Van Allen Probe A energetic particle, composition, and thermal plasma suite (ECT) helium oxygen proton electron, HOPE, mass spectrometer pitch angle resolved science data. Electron fluxes, 15 eV to 50 keV, and ion fluxes, 1 eV to 50 keV, as measured in alternate spin cadence, level 3, release 4 (L3), 11.35 s data [Dataset]. NASA Space Physics Data Facility. <https://doi.org/10.48322/17p9-rf75>

Funsten, H. O., Skoug, R. M., Guthrie, A. A., MacDonald, E. A., Baldonado, J. R., Harper, R. W., et al. (2013). Helium, oxygen, proton, and electron (HOPE) mass spectrometer for the radiation belt storm probes mission. *Space Science Reviews*, 179(1–4), 423–484. <https://doi.org/10.1007/s11214-013-9968-7>

Ganushkina, N. Y., Swiger, B., Dubyagin, S., Matéo-Vélez, J. C., Liemohn, M. W., Sicard, A., & Payan, D. (2021). Worst-case severe environments for surface charging observed at LANL satellites as dependent on solar wind and geomagnetic conditions. *Space Weather*, 19(9), e02732. <https://doi.org/10.1029/2021SW002732>

Gjerloev, J. W. (2012). The SuperMAG data processing technique. *Journal of Geophysical Research: Space Physics*, 117(A9), A09213. <https://doi.org/10.1029/2012JA017683>

Grand, R., Knott, K., & Pedersen, A. (1983). Spacecraft charging effects. *Space Science Reviews*, 34(3), 289–304. <https://doi.org/10.1007/BF00175284>

Koons, H. C., Mazur, J. E., Selesnick, R. S., Blake, J. B., & Fennell, J. F. (1999). The impact of the space environment on space systems. Technical Report, AD-A376872; TR-99(1670)-1; SMC-TR-00-10 EL Segundo Technical Operations.

Lai, S. T. (2003). A critical overview on spacecraft charging mitigation methods. *IEEE Transactions on Plasma Science*, 31(6), 1118–1124. <https://doi.org/10.1109/TPS.2003.820969>

Lai, S. T., & Della-Rose, D. J. (2001). Spacecraft charging at geosynchronous altitudes: New evidence of existence of critical temperature. *Journal of Spacecraft and Rockets*, 38(6), 922–928. <https://doi.org/10.2514/2.3764>

Lai, S. T., & Tautz, M. (2006a). High-level spacecraft charging in eclipse at geosynchronous altitudes: A statistical study. *Journal of Geophysical Research: Space Physics*, 111(A9), A09201. <https://doi.org/10.1029/2004JA010733>

Lai, S. T., & Tautz, M. F. (2006b). Aspects of spacecraft charging in sunlight. *IEEE Transactions on Plasma Science*, 34(5), 2053–2061. <https://doi.org/10.1109/TPS.2006.883362>

Lanzerotti, L. J., Breglia, C., Maurer, D. W., Johnson, G. K., & MacLennan, C. G. (1998). Studies of spacecraft charging on a geosynchronous telecommunications satellite. *Advances in Space Research*, 22(1), 79–82. [https://doi.org/10.1016/S0273-1177\(97\)01104-6](https://doi.org/10.1016/S0273-1177(97)01104-6)

Li, W., Thorne, R. M., Nishimura, Y., Bortnik, J., Angelopoulos, V., McFadden, J. P., et al. (2010). THEMIS analysis of observed equatorial electron distributions responsible for the chorus excitation. *Journal of Geophysical Research: Space Physics*, 115(1), A00F11. <https://doi.org/10.1029/2009JA014845>

Loto'aniu, T. M., Singer, H. J., Rodriguez, J. V., Green, J., Denig, W., Biesecker, D., & Angelopoulos, V. (2015). Space weather conditions during the Galaxy 15 spacecraft anomaly. *Space Weather*, 13(8), 484–502. <https://doi.org/10.1002/2015SW001239>

Matéo-Vélez, J. C., Sicard, A., Payan, D., Ganushkina, N., Meredith, N. P., & Sillanpää, I. (2018). Spacecraft surface charging induced by severe environments at geosynchronous orbit. *Space Weather*, 16(1), 89–106. <https://doi.org/10.1002/2017SW001689>

Mauk, B. H., Fox, N. J., Kanekal, S. G., Kessel, R. L., Sibeck, D. G., & Ukhorskiy, A. (2013). Science objectives and rationale for the radiation belt storm probes mission. *Space Science Reviews*, 179(1–4), 3–27. <https://doi.org/10.1007/s11214-012-9908-y>

Meredith, N. P., Horne, R. B., Thorne, R. M., Summers, D., & Anderson, R. R. (2004). Substorm dependence of plasmaspheric hiss. *Journal of Geophysical Research: Space Physics*, 109(A6), A06209. <https://doi.org/10.1029/2004JA010387>

Moore, T. E., Arnoldy, R. L., Feynman, J., & Hardy, D. A. (1981). Propagating substorm injection fronts. *Journal of Geophysical Research*, 86(A8), 6713–6726. <https://doi.org/10.1029/JA086iA08p06713>

Mullen, E. G., Gussenhoven, M. S., & Garrett, H. B. (1981). A worst case spacecraft environment as observed by SCATHA on 24 April 1979.

Mullen, E. G., Gussenhoven, M. S., Hardy, D. A., Aggson, T. A., Ledley, B. G., & Whipple, E. (1986). SCATHA survey of high-level spacecraft charging in sunlight. *Journal of Geophysical Research*, 91(A2), 1474–1490. <https://doi.org/10.1029/JA091iA02p01474>

NASA's Space Physics Data Facility (SPDF) Website. (2023). NASA's space physics data facility (SPDF) [Dataset]. Retrieved from <https://spdf.gsfc.nasa.gov/pub/data/rbsp/>

Newell, P. T., & Gjerloev, J. W. (2011). Evaluation of SuperMAG auroral electrojet indices as indicators of substorms and auroral power. *Journal of Geophysical Research: Space Physics*, 116(A12), A12211. <https://doi.org/10.1029/2011JA016779>

Olsen, R. C. (1983). A threshold effect for spacecraft charging. *Journal of Geophysical Research Supplement*, 88(A1), 493–499. <https://doi.org/10.1029/JA088iA01p00493>

Reagan, J. B., Meyerott, R. E., Gaines, E. E., Nightingale, R. W., Filbert, P. C., & Imhof, W. L. (1983). Space charging currents and their effects on spacecraft systems. *IEEE Transactions on Electrical Insulation*, 18(3), 354–365. <https://doi.org/10.1109/TEL.1983.298625>

Rosen, A. (1976). Spacecraft charging by magnetospheric plasmas. *IEEE Transactions on Nuclear Science*, 23(6), 1762–1768. <https://doi.org/10.1109/TNS.1976.4328575>

- Sarno-Smith, L. K., Larsen, B. A., Skoug, R. M., Liemohn, M. W., Breneman, A., Wygant, J. R., & Thomsen, M. F. (2016). Spacecraft surface charging within geosynchronous orbit observed by the Van Allen Probes. *Space Weather*, *14*(2), 151–164. <https://doi.org/10.1002/2015SW001345>
- Shan, X., Miao, B., Cao, Z., Sun, Z., Li, Y., Liu, K., et al. (2023a). First results of the low energy ion spectrometer onboard a Chinese geosynchronous satellite. *Science in China E: Technological Sciences*, *66*(5), 1378–1384. <https://doi.org/10.1007/s11431-022-2143-6>
- Shan, X., Miao, B., Cao, Z., Sun, Z., Li, Y., Liu, K., et al. (2023b). A low-energy ion spectrometer with large field of view and wide energy range onboard a Chinese GEO satellite. *Open Astronomy*, *32*(1), 210. <https://doi.org/10.1515/astro-2022-0210>
- Spence, H. E., Reeves, G. D., Baker, D. N., Blake, J. B., Bolton, M., Bourdarie, S., et al. (2013). Science goals and overview of the radiation belt storm probes (RBSP) energetic particle, composition, and thermal plasma (ECT) suite on NASA's Van Allen Probes mission. *Space Science Reviews*, *179*(1–4), 311–336. <https://doi.org/10.1007/s11214-013-0007-5>
- Spence, H. E., Reeves, G. D., & Blake, J. B. (2022). Van Allen Probe A energetic particle, composition, and thermal plasma suite (ECT) magnetic electron ion spectrometer (MagEIS), electron fluxes, 20 to 4000 keV, proton fluxes, 60 to 1500 keV, level 3, release 4 (L3), 10.9 s data [Dataset]. <https://doi.org/10.48322/09qz-tf17>
- SuperMAG Website. (2023). SuperMAG electrojet (SME) index [Dataset]. Retrieved from <https://supermag.jhuapl.edu/indices/>
- Thomsen, M. F., Denton, M. H., Lavraud, B., & Bodeau, M. (2007). Statistics of plasma fluxes at geosynchronous orbit over more than a full solar cycle. *Space Weather*, *5*(3), 03004. <https://doi.org/10.1029/2006SW000257>
- Thomsen, M. F., Henderson, M. G., & Jordanova, V. K. (2013). Statistical properties of the surface-charging environment at geosynchronous orbit. *Space Weather*, *11*(5), 237–244. <https://doi.org/10.1002/swe.20049>